Enhancing magnetic properties in Mn_{3}Ge thin films by doping

Jan Balluff, Jan-Michael Schmalhorst, Elke Arenholz, Markus Meinert, and Günter Reiss

Phys. Rev. B **97**, 014403 — Published 3 January 2018

DOI: 10.1103/PhysRevB.97.014403

Enhancing magnetic properties in Mn_3Ge thin films by doping

Jan Balluff,[1,*] Jan-Michael Schmalhorst,[1] Elke Arenholz,[2] Markus Meinert,[1,†] and Günter Reiss[1]

[1] *Center for Spinelectronic Materials and Devices, Bielefeld University, D-33501 Bielefeld, Germany*

[2] *Advanced Light Source, Lawrence Berkeley National Laboratory, CA 94720, USA*

(Dated: December 12, 2017)

The ferrimagnetic Mn_3Ge compound has appealing properties for spintronic applications, e.g., a low saturation magnetization and often a large coercive field is found. Here, we report on a combined experimental and theoretical approach to both reduce the magnetization and increase the coercivity of Mn_3Ge by doping. By calculating defect formation energies we predict several dopants that are expected to specifically occupy only one lattice site of the crystal structure. For Ni as a dopant, we predict a reduction in the magnetization which we verify by preparing thin film samples by magnetron co-sputtering. We confirm the predicted reduction in magnetization as well as a greatly enhanced coercivity of more than 5 T. To improve the understanding of the sublattice magnetization in the doped ferrimagnetic material, we performed magnetic spectroscopy experiments on selected samples and compare the results with calculated data. An important finding from a detailed analysis of the spectroscopic data is that a frequently observed soft contribution in the magnetization loop arises from impurities in the film.

I. INTRODUCTION

Magnetic materials play a key role within the field of spintronics. To realize a memory element or a sensor based on magnetic tunnel junctions[1,2], several materials with specific magnetic properties are required. One of them is a reference layer with a fixed magnetization. This is commonly achieved by the exchange bias[3,4] in bilayers of a ferromagnet and an antiferromagnet that creates a shift of the magnetic hysteresis along the field axis and a well-defined reference state at zero field. Second, a magnetically free layer is required that can be easily manipulated by external fields or spin polarized currents using the spin transfer torque[5,6]. To achieve a large tunneling magnetoresistance, a high spin polarization is desirable. Furthermore, the miniaturization of such devices, e.g., in magnetic memories[7] needs small stray fields. The long list of requirements makes it a difficult task to find suitable materials for future mass production.

A promising candidate for low-moment and high anisotropy is the Mn_3Ge compound. Within the Mn-Ge phase diagram[8] the ϵ_1-phase, the body-centered tetragonal $D0_{22}$ structure (spacegroup $I4/mmm$, No. 139), is found in a narrow range of 76.5% - 78% atomic Mn content. The native composition of this phase therefore is $Mn_{3.4}Ge$, however, by forced epitaxy in thin film, the $D0_{22}$ structure can be obtained also with slightly different compositions, e.g., Mn_3Ge. This ferrimagnetic compound, whose structure is shown in Fig. 1(a), has two magnetically distinct sublattices, denoted by their Wyckoff positions as Mn_{2b} and Mn_{4d}. It was investigated by several groups during the recent years with a focus on its applicability in spintronic devices[9–11]. Mn_3Ge has a low saturation magnetization of about $1\,\mu_B$ per formula unit (f.u.) resulting in weak stray fields[9,12], which facilitates an application as an electrode material in magnetic tunnel junctions. Theoretical work of Miura *et al.* predicts a large spin polarization for the Mn_3Ge stoichiometry, which would lead to a large magnetoresistance[14].

On the other hand, the coercivity of this compound can be of the order of 2 T and depends on the content of Mn. A material of large coercivity could replace the commonly used exchange biased reference layer in magnetic tunnel junctions. Due to the supply risk of iridium, which is often used in the form of the antiferromagnetic IrMn to obtain the exchange bias[15], a suitable replacement will be needed in the near future.

In the present work, we investigate the effect of doping on the magnetic properties of the Mn_3Ge compound. In a first step, we computed the effects of replacing a single Mn atom with another element. For Ni, we find a promising reduction in the magnetization and predict a stable substitution. Therefore, in a second step, we prepared thin film Mn_3Ge samples doped with different amounts of Ni using magnetron co-sputtering. The samples were magnetically characterized and X-ray magnetic circular dichroism (XMCD)[16] on selected samples was used to get a detailed insight into the internal magnetic sublattice structure.

II. METHODS

In a first step we investigate the Mn_3Ge compound using density functional theory (DFT). We utilize the Vienna Ab initio Simulation Package (VASP)[17–19], an implementation of the projector augmented plane waves (PAW) framework[20] with the generalized gradient approximation (GGA) using the PBE exchange correlation functional[21]. We use a $2 \times 2 \times 2$ unit cell containing 32 atoms of which 24 are Mn. In two separate calculations we investigate the effect of replacing a single Mn atom on one of the sublattices with a dopant element Z. The resulting composition is $Mn_{2.875}Z_{0.125}Ge$ (MZG). The initial magnetic moments are set according to Hund's rule, where the magnetic moments of the $2b$ and $4d$ sublat-

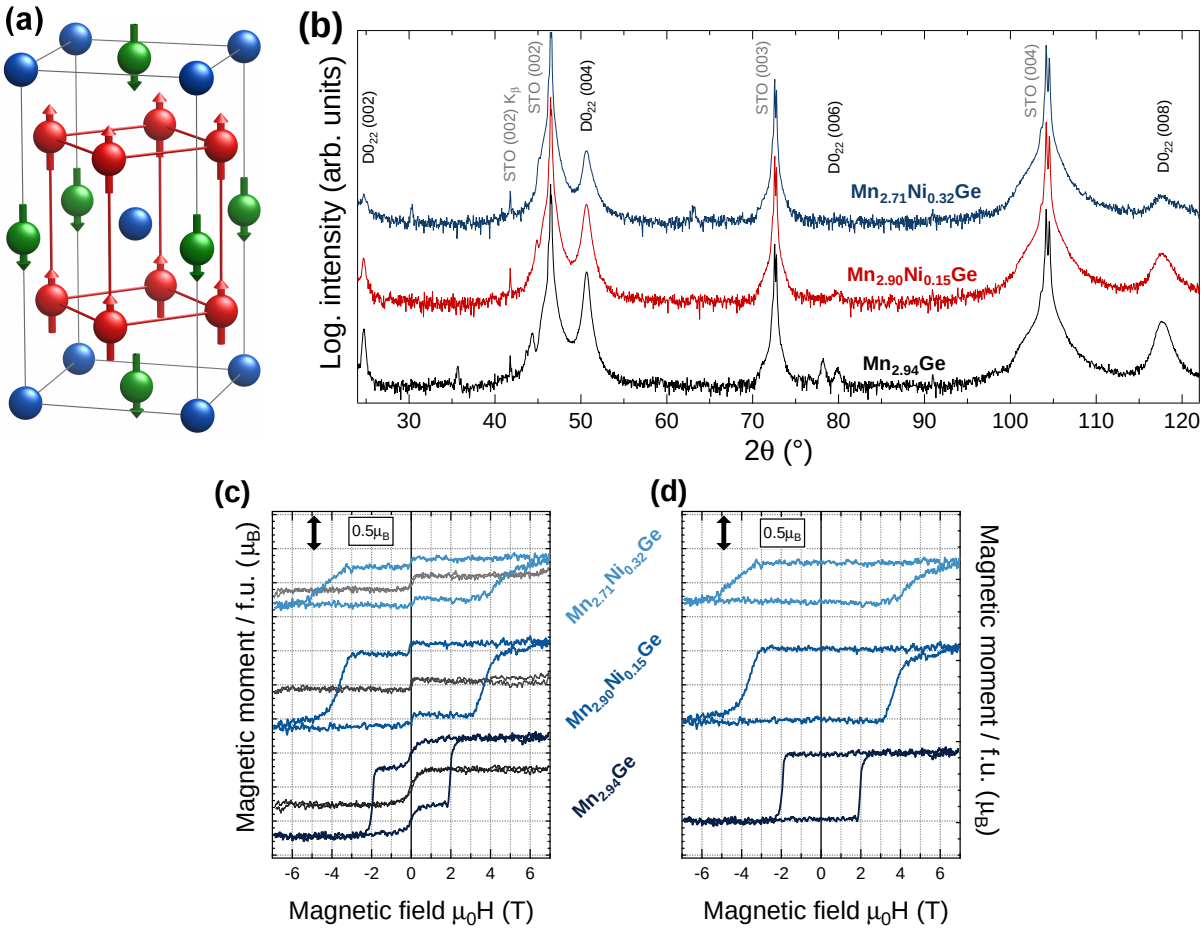

FIG. 1. (a): $D0_{22}$ crystal structure. Wyckoff position $2a$ is occupied by Ge (blue), whereas Mn occupies positions $2b$ (green) and $4d$ (red). Arrows indicate the ferrimagnetic configuration. Created with VESTA[24]. (b): X-ray diffraction patterns for doped and undoped Mn_3Ge. (c) and (d): Hysteresis loops for Ni doped Mn_3Ge. On the y-axis, the magnetic moment per formula unit is plotted in units of μ_B, where one major tick is equivalent to $0.5\,\mu_B \hat{=} 87.7\,kA/m$. Raw data is plotted in (b) with the field oriented out-of-plane in blue and in-plane in gray. (c) shows the data with the softmagnetic contribution fitted and removed using a Langevin function. All data is corrected for the diamagnetic contribution of the substrate.

tices are set antiparallel. The plane wave cutoff is 450 eV and the integration of the Brillouin zone is done at a Γ-centered **k**-point mesh of $7\times7\times7$ using the tetrahedron method with Blöchl corrections[22]. We calculate the defect formation energy of an element for both sublattices separately by

$$\Delta E_D = 8E(\mathrm{MZG}) - 8E(\mathrm{Mn_3Ge}) + E(\mathrm{Mn}) - E(\mathrm{Z})\,, \quad (1)$$

where $E(X)$ is the total energy of X. If ΔE_D is negative, the structure is stabilized by the dopant and it is assumed that the dopant will not segregate from the structure.

In the second step, we prepared thin film samples for one of the candidates with $\Delta E_D < 0$: Ni. The samples were prepared using magnetron co-sputtering from elemental targets. The base pressure of the vacuum chamber was better than 10^{-8} mbar. High purity Ar was used as a sputtering gas and the deposition pressure was 2×10^{-3} mbar. Samples were grown on $SrTiO_3$ substrates (STO) at a substrate temperature of 500°C. The lattice mismatch with the STO substrate is as low as 2.4% ($a_{STO} = 3.91$Å) with the a-direction of the $D0_{22}$ structure, therefore the samples grow with the c-direction oriented perpendicular to the substrate surface. After cooling down the samples, a protective layer of about 2 nm Si was deposited at ambient temperature. The composition of the samples was determined by X-ray fluorescence and energy dispersive X-ray spectroscopy. This analysis is typically accurate within 1% atomic content. Doping was achieved by co-sputtering the dopant material and simultaneously reducing the Mn sputtering power to keep the (Mn,Z):Ge ratio fixed.

The crystalline growth of the $D0_{22}$ structure was confirmed by X-ray diffraction measurements. The thickness of the $Mn_{3-x}Z_xGe$ films was determined by X-ray reflectivity at small angles and fitting the data with the Parratt algorithm[23]. The magnetic characterization was done using a vibrating sample magnetometer (VSM) providing a

TABLE I. Calculated values for different dopant elements Z, where Z=Mn refers to the native Mn_3Ge compound. Denoted are the doped sublattice, the defect formation energy ΔE_D for doping this sublattice, the total magnetization m_{tot} and the average magnetic moment per Mn atom for each sublattice m_{2b}(Mn) and m_{4d}(Mn) as well as the magnetic moment of the dopant atom m_Z. Note that the total magnetization m_{tot} differs slightly from sums of the sublattice magnetizations, because the Ge atoms and the interstitial region between the PAW spheres have small magnetic moments.

Dopant Z	Sublattice	ΔE_D (eV)	m_{tot} (μ_B/f.u.)	m_{2b}(Mn) (μ_B/ Mn atom)	m_{4d}(Mn) (μ_B/ Mn atom)	m_Z (μ_B/ Z atom)
Mn	—	—	1.03	-2.89	1.99	—
Ti	2b	-0.309	1.38	-2.91	2.02	-0.64
V	2b	-0.240	1.28	-2.91	2.00	-1.12
Ni	4d	-0.022	0.68	-2.91	1.95	-0.31
Rh	4d	-0.311	0.82	-2.93	1.71	0.01
Ir	4d	-0.130	0.83	-2.92	1.70	0.10
Pt	4d	-0.143	0.71	-2.96	1.67	-0.07

maximum field of 7 T. The samples were cut down to approximately $5\times5\,mm^2$, where the exact sample area was determined with a microscope and digital image processing. All samples were characterized with the magnetic field oriented in the plane as well as out-of-plane.

The magnetic spectroscopy measurements on selected samples were done at beamline 4.0.2 of the Advanced Light Source (Berkeley, US). Two separate pieces of each sample were magnetized in ±7 T prior to measurements to set two opposite remanent magnetic states. X-ray absorption (XA) spectra were recorded for different orientations between helicity and magnetization, $\alpha^+(E)$ and $\alpha^-(E)$, and the resulting XMCD signal $\alpha^+(E)-\alpha^-(E)$ was averaged over all possible combinations. The absorption was measured in the total electron yield, where the drain current caused by secondary electrons escaping from the sample is measured.

To improve our understanding of the ferrimagnetic substructure and test our interpretation of the results we calculated the XMCD spectrum for the Mn_3Ge structure using density functional theory. The full dielectric tensor was computed in the full-potential linearized augmented plane-wave (FLAPW) program ELK.[25] Here, the $2p$ core levels were described as valence states by local orbitals and an automatically optimized linearization energy. The spin-orbit coupling of the valence states was treated with a second-variational scheme. Dense **k**-point meshes of $20\times20\times20$ points were used to obtain the dielectric tensor. The XMCD signal was then obtained as $\mathrm{XMCD}(E)=\alpha^+(E)-\alpha^-(E)$, where the absorption coefficient α was computed using the standard formalism, i.e., $\alpha^\pm=(2\omega/c)\,\mathrm{Im}\left(\sqrt{\varepsilon^\pm}\right)$. The ±-components were obtained as $\varepsilon^\pm=\varepsilon_{xx}\pm\varepsilon_{xy}$, assuming tetragonal symmetry with the X-rays incident along the z-axis, in agreement with the experimental condition.

III. RESULTS

The investigation of defect formation energies ΔE_D was done for all elements except the ones from main groups I, II, VII, and VIII, as well as radioactives and rare earth metals. The results predict $\Delta E_D<0$ for doping with Ti or V on sublattice $2b$ and for Ni, Rh, Ir, or Pt on sublattice $4d$. The results for these six dopant elements are summarized in Table I. The values for ΔE_D are all in the range of -100 to -300 meV except for Z=Ni, where $\Delta E_D=-22$ meV is found. In addition to ΔE_D we compare the magnetic moments of the different elements and sublattices. A general result found in all calculations is an increased (decreased) total magnetization when doping sublattice $2b$ ($4d$). Therefore, we predict a stable structure with increased magnetization for Z = (Ti, V) and with decreased magnetization for Z = (Ni, Rh, Ir, Pt).

The average magnetic moment m_{2b}(Mn) and m_{4d}(Mn) of the Mn atoms on both sublattices are only slightly affected by the doping in general. For Z=(Rh, Ir, Pt) we find a slightly reduced magnetic moment on the $4d$ Mn atom. Due to the small magnetic moments of the dopant atoms, however, we find a visible effect on the total magnetization m_{tot}. Compared to the reference value of 1.03 μ_B/f.u. for the native Mn_3Ge, we find an increase for $Mn_{2.875}Z_{0.125}Ge$ of up to 134% for Z=Ti and a decrease down to 66% for Z=Ni, which is in agreement with an investigation by You and coworkers[26]. As Z=Ni is predicted to generate the largest reduction in the magnetization, we chose Ni as a dopant material for our experimental investigation.

We prepared a series of samples with different Ni content, where the (Mn,Ni):Ge ratio was kept at 3:1 as close as possible. X-ray diffraction analysis of the sputtered films verified the crystallization of the $D0_{22}$ structure. Corresponding diffraction patterns of the samples discussed here are shown in Fig. 1. The lattice parameter obtained from the diffraction peaks is $c=7.21$ Å in

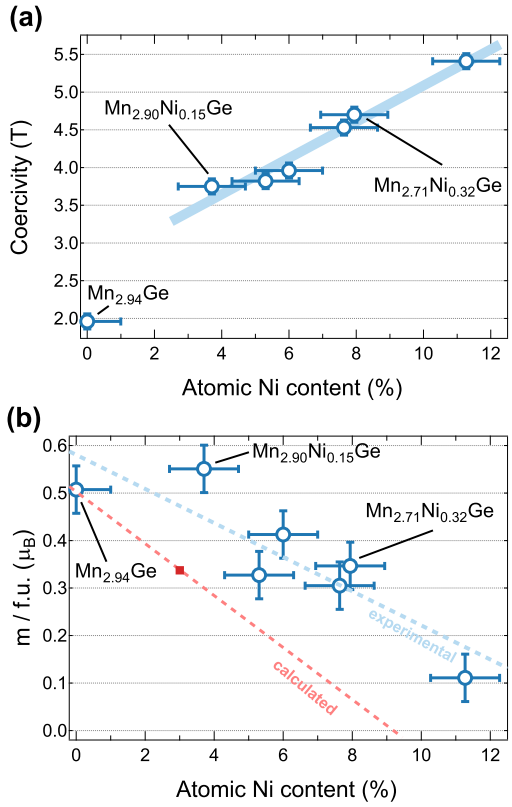

FIG. 2. Coercivity and magnetization depending on the Ni concentration. Values are extracted after removing the soft-magnetic contribution. (a): The coercivity is proportional to the Ni concentration as indicated by the shaded line. (b): The saturation magnetization shows a decreasing linear trend when increasing the Ni concentration. The red marker and dashed line show the linearly extrapolated magnetization obtained from DFT scaled to match the experimental value of the $Mn_{2.94}Ge$ sample.

good agreement with the results obtained for bulk Mn_3Ge ($c_{bulk} = 7.261$ Å[12]). It did not change visibly when doping with Ni up to $Mn_{2.71}Ni_{0.32}Ge$. The peak intensity of the $D0_{22}$ structure is slightly reduced for large Ni content. The thickness for the samples was determined using X-ray reflectivity and was 48 nm for all samples.

The magnetic analysis using a VSM is shown exemplarily for three samples in Fig. 1(c) and (d). The first graph (Fig. 1(c)) shows the raw magnetization loop given as the magnetic moment per formula unit, where the diamagnetic contribution of the substrate was removed. Measurements with the field oriented in the sample plane are plotted in blue, and with the field oriented out-of-plane are plotted in gray. The data show several interesting features. First of all, a soft-magnetic contribution is found both in in-plane and in out-of-plane hysteresis loops. As the Mn_3Ge usually has a strong out-of-plane anisotropy, we do not attribute this contribution to the $D0_{22}$ phase. It is most likely caused by impurity phases, which is supported by the occurence of additional peaks in the X-ray diffraction spectrum, which can not be indexed with the $D0_{22}$ phase. The magnetic switching of the $Mn_{3-x}Z_xGe$ compound is found as the second, hard-magnetic contribution for all samples in the out-of-plane direction. By fitting the soft-magnetic contribution in the out-of-plane loops with a Langevin function and removing it we isolate the hardmagnetic hysteresis, which is plotted in Fig. 1(d). The saturation magnetization differs by a factor of 2 from the calculated values, which is yet to be understood. Similar results are found by Sugihara and co-workers[11]. The result can be understood in part by the fact that the exact volume fractions of hard- and soft-magnetic contributions is not known and we obtained the magnetization by normalizing the magnetic moment with the full film volume, which obviously leads to an underestimated magnetization of the $D0_{22}$ fraction. Furthermore, it can be expected that Mn-Ge disorder also leads to a reduced magnetization.

The addition of Ni greatly enhances the coercivity. This is shown for all samples of the series in Fig. 2. In Fig. 2(a) the coercivity is plotted as a function of the Ni concentration in the compound. The graph shows a linearly increasing coercivity, indicated by the shaded line, up to 5.41 T when doping the Mn_3Ge compound with Ni. In the second graph in Fig. 2(b), the saturation magnetization extracted from Fig. 1(d) is plotted as a function of the Ni concentration. It turns out that the addition of Ni significantly reduces the magnetization as predicted by the DFT calculation. Albeit achieving full reproducibility of the magnetic properties of the Mn-Ge films is difficult, as indicated by the scattering, a larger number of prepared samples with similar stoichiometries ensure that our results are not an artifact of reproducibility errors.

For the investigated composition the formation of Ni clusters is improbable. If Ni forms clusters or impurity phases these would most likely be ferromagnetic or, at least, ferrimagnetic. We should clearly see this in the measurement as an increase in signal amplitude, because the saturation magnetization of Ni is larger by a factor of about 10 compared to our samples. This is not observed, thus we conclude that the observed results are due to the Ni doped into the $D0_{22}$ phase. We find a steadily decreasing magnetization with increasing Ni concentration, however, the scatter of the data is much larger than for the coercivity. The red marker and the dashed red line in the graph show the expected magnetization based on the DFT results. Here it is assumed that Ni would only enter the 4*d* sites and that the sublattice magnetic moments are independent of the Ni concentration. In addition, the line was scaled to match the experimental magnetization of the $Mn_{2.94}Ge$ sample. The steadily decreasing magnetization is in agreement with our prediction as well as the one by You et al. for larger Ni concentrations[26]. However, we observe that the reduction of the magnetization with increased Ni content is not as strong as expected from the calculation, which may indicate that th Ni atoms do not solely occupy the 4*d* sites. In particular, one would expect full compensation close to a Ni content

of 9%, whereas the experimental curve indicates that full compensation can be expected around 15% of Ni content. We find a decrease in magnetization with increasing Ni content and simultaneously an increase in coercivity. Because the magnetization decreases more than the coercivity increases, the energy product of the hysteresis slightly decreases in this doping concentration range.

To understand the sublattice magnetization in doped Mn_3Ge, we investigated the samples discussed in Fig. 1 using magnetic spectroscopy at beamline 4.0.2 of the Advanced Light Source. In order to separate the different magnetic contributions we used two approaches: in the first approach, the additive approach, we measured the XMCD signal at +0.3 T and -0.3 T both in the back and the forth loops of the hysteresis. This is achieved by saturating two separate pieces of the same sample in a magnetic field of +7 T and -7 T, respectively, prior to the X-ray measurement. Denoting the softmagnetic saturation value as M^* and the hardmagnetic one as M, this yields four absorption spectra, namely $M \pm M^*$ and $-M \pm M^*$. Thus, the two contributions can be separated algebraically. This approach is depicted in Fig. 3(a). In a second approach, the separative approach, we separated the contributions geometrically by rotating the softmagnetic contribution perpendicular to the hardmagnetic contribution using an external magnetic field of 0.3 T. This geometry is depicted in Fig. 3(b). As the XMCD signal is only sensitive to the magnetization parallel to the incident X-rays, the two contributions can be measured separately. The sample is tilted against the incident X-rays in both cases. When probing M, M^* is oriented perpendicular to M using an external magnetic field $\mathbf{B}$. This field would cause the secondary electrons to be redirected back onto the sample, so no electron yield would be measured. Therefore, we use an angle of $\theta = 70°$ between the sample plane and the incident X-rays in this measurement. In the other case, when probing M^*, the sample plane is parallel to the incident X-rays, where the beam would not hit the sample surface. Therefore, we use an angle of $\theta = 20°$.

We compare the resulting XMCD spectra in Fig. 3(c)-(e). All results are obtained from the XA spectra normalized to an absorption of 1 after the L_2 edge. The first graph, Fig. 3(c), shows the hardmagnetic contribution for an undoped $Mn_{2.94}Ge$ sample. We find a small XMCD signal with a pronounced substructure, which we interpret as a superposition of two distinct Mn XMCD spectra of slightly different shape originating from the two Mn sublattices in the ferrimagnetic sample. As the magnetic moments of the Mn atoms on the two sublattices differ, the two spectra do not cancel each other, resulting in the substructure we observe. We attribute an XMCD with positive (negative) sign at the L_3 edge to the Mn $4d$ ($2b$) sublattice. We measured this magnetic contribution with both approaches, where the results match precisely as shown in the graph, so we can clearly attribute the structure of this XMCD spectrum to the Mn_3Ge compound. This is supported by the investigation of the softmagnetic contribution shown in Fig. 3(d). We also observe matching spectra from both methods, however, they do not show any distinct substructure. We therefore conclude that the softmagnetic contributions in our samples do not originate from the $D0_{22}$ structure of the ferrimagnetic Mn_3Ge compound.

In the last graph, Fig. 3(e), we compare the results for different Ni concentrations. In gray, the signal for the undoped reference sample is plotted. For a small Ni concentration, plotted in orange, we find peak B greatly reduced and peak A slightly enhanced. We explain this by the Ni doping reducing the $4d$ sublattice magnetization resulting in the reduction of the positive contribution to the spectrum. In the case of larger Ni concentration, we find a weak reduction in the XMCD signal for the whole spectrum. This single-spot XMCD analysis agrees quantitatively with the bulk-sensitive VSM measurement. Therefore, as we are able to separate the magnetic contributions in both measurements, the observed results show that the effects are intrinsic for the Ni doping.

The unspecific reduction of the XMCD signal is probably related to the Ni atoms not specifically entering the $4d$ lattice sites, but randomly occupying all lattice sites at larger concentration. To further validate this interpretation, we measured the XMCD signal of Ni. The XMCD signal at the Ni L_3 edge for this sample is plotted in the right part of Fig. 3(e). The positive signal indicates an orientation of the Ni moment parallel to the Mn_{4d} moments, which is contrary to our calculation, but supports the previous interpretation that Ni randomly dissolves in the lattice at higher concentrations. Although the formation energy for Ni substitutions on $2a/b$ sites is positive, the high-temperature growth and the associated entropy of mixing can make these unfavorable substitutions feasible. However, due to the small concentrations and thus small difference $\alpha^+(E) - \alpha^-(E)$, this analysis was only possible for the largest Ni concentration and a quantitative interpretation is not possible.

In Fig. 4 we present the computed XMCD spectra resolved by the individual contributions to the XMCD of the structurally inequivalent Mn atoms on Wyckoff $2b$ and $4d$ positions. Naturally, the two XMCD signals have opposite sign because of the antiparallel alignment of the magnetic moments. However, the two XMCD spectra from the $2b$ and $4d$ positions have different shape and amplitude, so that an oscillatory total signal remains, similar to our earlier findings on the inverse Heusler compound Mn_2CoGa.[27] The observed peaks in the spectrum, denoted as A-F in Fig. 4 (b), can now be assigned to the two positions. Peaks A, C, and E arise from the Mn $2b$ position, whereas peaks B and F can be assigned to Mn $4d$. The oscillatory structure D is not easily assigned to any one of the two positions. An important difference between the calculated and the observed spectra is that the experimental spectrum has a larger $3d$ band width, which is a commonly seen feature and originates from an incomplete description of the band structure by the

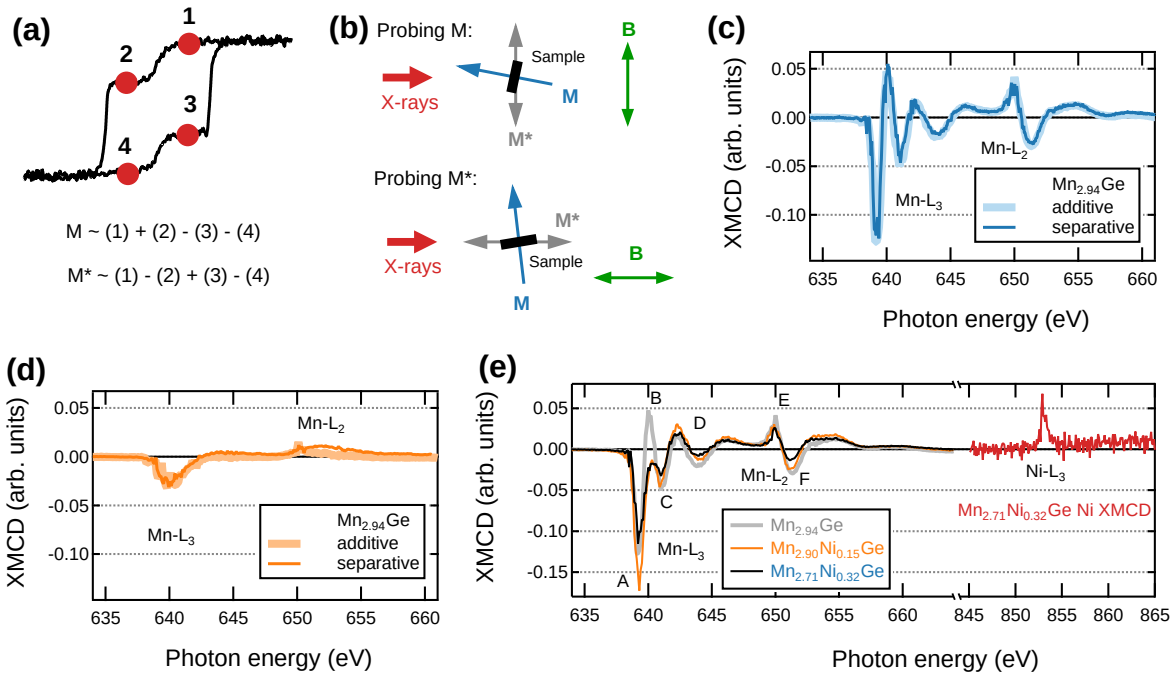

FIG. 3. XMCD analysis of Ni-doped Mn_3Ge. (a): Additive approach of probing M and M^* separately measuring at four different positions in the hysteresis. (b): Separative approach of probing the contributions using a perpendicular orientation of M and M^*. (c): XMCD of the hardmagnetic contribution of an undoped sample. Measurements using both approaches are plotted. (d): XMCD of the softmagnetic contribution of the same sample. (e): Comparison of the hardmagnetic XMCD signal for different Ni concentrations. Plotted data is obtained using the additive approach. Peaks B and F in the spectrum of the highest Ni concentration exhibiting a slightly larger reduction in amplitude compared to the overall spectrum. Additionally plotted in red is the Ni XMCD signal at the L_3 edge for this sample.

Kohn-Sham bands in DFT. Furthermore, the XMCD at the L_3 resonance is larger than the XMCD at the L_2 resonance, in contrast to the calculation. This can be traced back to a slightly larger spin-orbit splitting of the $2p$ levels in the calculation for the Mn $4d$ atoms as compared to Mn $2b$, which seems to be incorrect. With a smaller spin-orbit splitting, the total signal would obviously be reduced without affecting the shape of the L_3 spectrum. However, the relative alignment of the orbitals appears to be well reproduced by the calculation, and it supports the view that the observed hard-magnetic contribution is intrinsic to the Mn_3Ge, whereas the smooth soft-magnetic contribution can be assigned to impurities.

IV. CONCLUSION

We investigated the magnetic properties of $D0_{22}$ Mn_3Ge. Using density functional theory to calculate defect formation energies we were able to predict six elements as stable dopants of the Mn_3Ge crystal structure. For two of these, we predict an increase in magnetization and for the other four a decrease. For Ni, which we predict to reduce the magnetization, we prepared a series of thin film samples and measured the magnetic hysteresis. We find a linear increase in coercivity up to 5.41 T for the largest Ni concentration. Furthermore, the magnetization reduces as predicted.

In order to understand the internal ferrimagnetic structure and the prominent softmagnetic contribution we measured the XMCD of selected samples. Using two different approaches we were able to separate the softmagnetic and hardmagnetic contributions and investigate them separately. We find a pronounced substructure in the XCMD signal for the hardmagnetic part attributed to the ferrimagnetic structure with two sublattices of opposite magnetization direction. This substructure is not visible for the softmagnetic part. Therefore, we conclude that the softmagnetic contribution does not originate from the $D0_{22}$ Mn_3Ge itself, but from secondary impurity phases, which are often found among Mn based $D0_{22}$ systems.

Our investigation of the XMCD spectra for different Ni concentrations are in agreement with our hysteresis measurements and calculations. Noticeably, we find the Ni moment oriented antiparallel to the average Mn moment as predicted by our calculations. The sublattice Ni occupies, however, cannot be extracted from these measurements. In addition to our experiments we calculated the XMCD spectra. A comparison of the contributions we obtain for the two different Mn positions is in agreement with the experimental data. It supports our in-

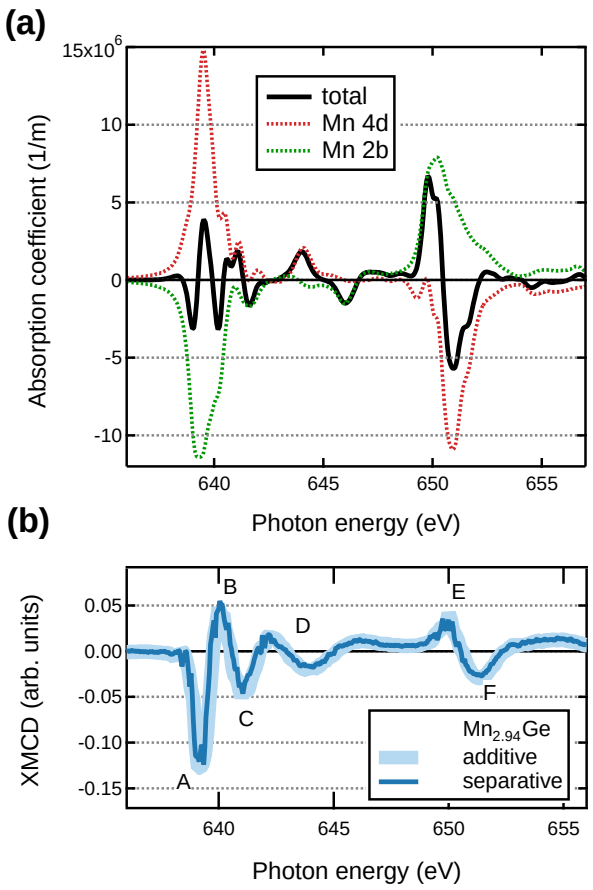

FIG. 4. Comparison of computed and observed XMCD signals. (a): Calculated XMCD contributions from the Mn 2b and 4d atoms and the total calculated XMCD. A Lorentzian broadening of 0.54 eV was applied to all spectra and the spectra were shifted to match the experimental energy. (b): The XMCD measurements as shown in Fig. 3 (c) in comparison.

terpretation of the distinct substructure in the XCMD spectrum, which is caused by the superposition of signals originating from two antiferromagnetically coupled sublattices.

In summary, we find a good agreement between our calculations and the experimentally investigated thin film samples. We have shown that DFT is a very useful tool to identify possible doping candidates and to improve magnetic properties. In combination with experiments it allows tailoring the sublattice magnetization and change certain properties to improve the applicability of materials in spintronic devices. Mn_3Ge is a promising material, as its properties can be easily tuned as demonstrated by our investigations. Especially, the giant coercivity of more than 5 T for Ni-doped Mn_3Ge is promising, as it makes the material similarly insensitive to external magnetic fields as exchange biased ferromagnetic layers.

V. ACKNOWLEDGEMENT

The research leading to these results has received funding from the European Union Seventh Framework Programme (FP7/2007-2013) under grant agreement no. NMP3-SL-2013-604398.

This research used resources of the Advanced Light Source, which is a DOE Office of Science User Facility under contract no. DE-AC02-05CH11231.

* balluff@physik.uni-bielefeld.de
† meinert@physik.uni-bielefeld.de

[1] J. F. Gregg, I. Petej, E. Jouguelet and C. Dennis, J. Phys. D. Appl. Phys. **35**, R121 (2002).
[2] C. Chappert, A. Fert, and F. N. Van Dau, Nat. Mater. **6**, 813 (2007).
[3] W. H. Meiklejohn, and C. P. Bean, Phys. Rev. **105**, 904 (1957).
[4] J. Nogués, and I. Schuller, J. Magn. Magn. Mater. **192**, 203 (1999).
[5] J. C. Slonczewski, J. Magn. Magn. Mater. **159**, L1 (1996).
[6] L. Berger, Phys. Rev. B **54**, 9353 (1996).
[7] A. V. Khvalkovskiy et al., J. Phys. D: Appl. Phys. **46**, 074001 (2013).
[8] A. B. Gokhale and R. Abbaschian, Bull. Alloy Phase Diagrams **11**, 460 (1990).
[9] H. Kurt et al. Appl. Phys. Lett. **101**, 132410 (2012).
[10] S. Mizukami et al., Appl. Phys. Express **6**, 123002 (2013).
[11] A. Sugihara, K. Suzuki, S. Mizukami, and T. Miyazaki, J. Phys. D: Appl. Phys. **48**, 164009 (2015).
[12] G. Kádár and E. Krén, Int. J. Magn **1**, 143 (1971).
[13] H. B. Huang et al., J. Magn. Magn. Mater. **330**, 16 (2013).
[14] Y. Miura and M. Shirai, IEEE Trans. Magn. **50**, 1400504 (2014).
[15] A. Kohn et al., Sci. Rep. **3**, 2412 (2013).
[16] J. Sthr, J. Magn. Magn. Mater. **200**, 470 (1999).
[17] G. Kresse and J. Furthmüller, Phys. Rev. B **54**, 11169 (1996).
[18] G. Kresse and D. Joubert, Phys. Rev. B **59**, 1758 (1999).
[19] Vienna ab-initio simulation package. Version 5.3.5. http://www.vasp.at
[20] P. E. Blöchl, Phys. Rev. B **50**, 17953 (1994).
[21] P. Perdew, K. Burke, and M. Ernzerhof, Phys. Rev. Lett. **77**, 3865 (1996).
[22] P. E. Blöchl, O. Jepsen, and O. K. Andersen, Phys. Rev. B **49**, 16223 (1994).
[23] L. G. Parratt. Phys. Rev. **95**, 359 (1954).
[24] K. Momma, and F. Izumi, J. Appl. Crystallogr. **44**, 1272 (2011).
[25] http://elk.sourceforge.net, version 4.3.06 (2017).

[26] Y. You, G. Xu, F. Hu, Y. Gong, E. Liu, G. Peng, and F. Xu, J. Magn. Magn. Mater. **429**, 40 (2017).
[27] M. Meinert, J.-M. Schmalhorst, C. Klewe, G. Reiss, E. Arenholz, T. Böhnert, and K. Nielsch, Phys. Rev. B **84**, 132405 (2011).